CrystEngComm

PAPER

View Article Online
View Journal | View Issue

Published on 03 July 2018. Downloaded by China university of Petroleum (East China) on 8/25/2018 1:58:30 AM.

Check for updates

Cite this: *CrystEngComm*, 2018, **20**, 4313

Optimizing crystallinity and porosity of hierarchical $Ni(OH)_2$ through conformal transformation of metal–organic framework template for supercapacitor applications†

Haobing Zhang,[a] Ben Xu,*[a] Zhenyu Xiao,[a] Hao Mei,[a] Liangliang Zhang,[a] Yinfeng Han*[b] and Daofeng Sun[a]

Received 6th May 2018,
Accepted 29th June 2018

DOI: 10.1039/c8ce00741a

rsc.li/crystengcomm

MOFs (metal–organic frameworks) are widely utilized as both the templates and precursors to prepare nanomaterials as supercapacitor electrodes. However, traditional thermolysis routes are difficult to control and usually lead to collapse of the MOF skeletons, which hinders wider applications. Herein, we describe a simple and facile strategy for fabricating the $Ni(OH)_2$ hierarchical structure by the "conformal transformation" of one particular Ni-MOF through hydrolysis in the KOH aqueous solution. By controlling the concentration of KOH solution and the soaking time, the obtained $Ni(OH)_2$ nanomaterial possesses both optimized crystallinity and porosity, extremely beneficial for electron transportation and ion migration within the electrodes. Taking these advantages, the $Ni(OH)_2$ electrode presents a remarkable specific capacity of 830.6 C g^{-1}, and the fabricated all-solid state asymmetric supercapacitor presents a remarkable energy density of 37.8 W h kg^{-1} at a power density of 252.67 W kg^{-1}, which surpasses most $Ni(OH)_2$ based supercapacitor devices. After 15 000 cycles, the capacitance remains at over 93% of the initial value.

Introduction

It has been widely acknowledged that novel energy resources and energy storage techniques are urgently demanded in the near future due to the vast consumption of fossil fuels and the associated environmental issues. Electrochemical energy techniques, including lithium ion batteries,[1] fuel cells,[2] and supercapacitors,[3] are paid plenty of attention at present. Supercapacitors are one of the promising candidates due to their considerable power density and fair energy density and have been widely applied to portable devices and electrical vehicles.[4] Supercapacitors are usually classified into two categories, which are the EDLC (electrical double layer capacitor) and PC (pseudo capacitor), of which the charge storage mechanisms are based on the electrical double layer and the fast redox reaction near the interface between electrode and electrolyte, respectively.[5–9] Porous carbons are the most important EDLC electrode materials and have been commercially applied.[10] Although presenting an extremely fast power deliver and long cycling life, they suffer from poor energy densities. On the contrary, PC electrodes, such as RuO_2 and MnO_2, present better energy storage capabilities and are usually utilized to fabricate hybrid supercapacitors, which are composed of porous carbons as one electrode and PC materials as the other electrode, to improve the energy densities of the devices.[11–15] Cobalt and nickel based oxide and hydroxide used to be studied as PC electrodes; however, there has arisen a debate upon their PC behaviors. More recently, researchers have treated these as battery-type electrodes due to their variable capacitance *versus* scanning voltage and the diffusion-controlled charge storage process.[16–18] $Ni(OH)_2$ is one promising battery-type electrode material due to its large theoretical capacitance and low cost.[19] Many methods have been developed to prepare $Ni(OH)_2$ electrodes, and it is concluded that the capacitance highly depends on the electron transportation in the electrodes and ion access to the interfaces between electrodes and electrolytes.[20] Thus, it is significant for the $Ni(OH)_2$ electrode material to have a good crystallinity for a higher electron conductivity along with large electrochemically active surface areas and a proper porous morphology for easy ion access to electroactive sites.[21]

MOFs (metal–organic frameworks) are novel porous materials and have been widely studied.[22–26] They are constructed of metal centers connected by organic ligands to give a 3D periodic structure. Recently, it was reported that several Co-

[a] College of Science, China University of Petroleum (East China), Qingdao, Shandong 266580, P. R. China. E-mail: benxu@upc.edu.cn
[b] Department of Chemical and Chemical Engineering, Taishan University, Tai'an, Shandong, 271021, P. R. China. E-mail: han@tsu.edu.cn

† Electronic supplementary information (ESI) available. See DOI: 10.1039/c8ce00741a

Published on 03 July 2018. Downloaded by China university of Petroleum (East China) on 8/25/2018 1:58:30 AM.

and Ni-MOFs were utilized as both the precursors and self-sacrificing templates to prepare nanoporous metal hydroxides through hydrolysis.[27–30] In 2013, Miles *et al.* first reported that Co-MOF-71 could be "conformally" transformed (without a significant change in morphology) into porous cobalt hydroxide in a NaOH (as well as KOH and LiOH) aqueous solution.[31] Liu and Zhang *et al.* also prepared porous $Co(OH)_2$ using the Co-BPDC-MOF precursor through the hydrolysis process, which exhibited a high specific capacitance of 241.8 C g^{-1} at 0.1 A g^{-1}.[29] In our previous work, we successfully prepared UPC-9-$Co(OH)_2$ 3D hierarchical structure by conformally transforming UPC-9 in a KOH aqueous solution. Subsequently, UPC-9-Co_3O_4 was obtained by calcinating UPC-9-$Co(OH)_2$ at 350 °C and presented a specific capacitance of 448.4 C g^{-1} at 1 A g^{-1}, and furthermore, the organic ligands can be recycled with a recycling ratio of 85%.[32] Our unpublished work also demonstrates that MCF-35 can be conformally transformed into a 3D $Ni(OH)_2$ hierarchical structure, which is ideal for supercapacitor applications. The conformal hydrolysis process from MOFs to metal hydroxides is an ideal strategy to fabricate 3D hierarchical metal hydroxides due to the following advantages: i) the hydrolysis process is mild and easily-operational and -controllable, and therefore the crystallinity and the morphology can be regulated by optimizing the reaction conditions such as the soaking duration and pH value; ii) the pore structure constructed by the OH^- ions is expected to provide abundant paths and electroactive sites for the OH^- ion migration to active sites; iii) the dissolved ligands in the alkali aqueous solution can be recollected, drastically reducing the cost. Although the conformal hydrolysis strategy is a promising method, a thorough and deep investigation is still needed, especially the effects of hydrolyzing conditions on the electrochemical performances of the resultant electrodes.

In this paper, a **Ni-MOF** utilizing BTC (1,3,5-benzenetricarboxylic acid) as the ligand was hydrolyzed to porous $Ni(OH)_2$ by simply soaking it in KOH aqueous solutions with varied concentrations. The hydrolysis processes in KOH aqueous solutions with different concentrations were investigated. Our results indicate that the conformal transformation only occurs within a certain range of the KOH concentration. Furthermore, the effects of the immersion time on the crystallinity and porosity of $Ni(OH)_2$ were also studied to obtain the optimized conditions. The $Ni(OH)_2$ electrode prepared at the optimized condition exhibits a high specific capacity of 830.6 C g^{-1} at a current density of 0.5 A g^{-1} and maintains its 60% capacitance at 20 A g^{-1}. The fabricated hybrid supercapacitor presents a remarkable energy density of 37.8 W h kg^{-1} and power density of 252.67 W kg^{-1}. The capacitance remains over 93% after 15 000 cycles.

Experimental

Material characterizations

The XRD patterns were collected employing a Bruker AXS D8 Advance instrument with Cu-Kα radiation (λ = 1.5418 Å) over the 2-theta range from 3° to 75°. FTIR spectra were measured using a PerkinElmer Frontier FT-IR Spectrometer within the 4000–400 cm^{-1} region. Microstructural characteristics of the samples were observed using a scanning electron microscopy (SEM, JSM-7500F) and a transmission electron microscope (TEM, Tecnai G2F20). The specific surface areas of the powder samples were determined by N_2 adsorption–desorption measurement employing a surface area analyzer ASAP-2020. The chemical states were investigated using an X-ray photoelectron spectrometer (XPS, EscaLab 250Xi) with monochromated Al-Kα irradiation. Thermo-gravimetric analyses (TGA) experiments were carried out on a Mettler Toledo TGA instrument with a heating rate of 10 °C min^{-1} in the range 40–900 °C under a nitrogen flow.

Synthesis of the Ni-MOF

The preparation method of the **Ni-MOF** was reported in a previous article.[33] Nickelous carbonate (1.0 mmol, 0.1791 g) was gradually added to 10 mL of a boiling aqueous solution of H_3BTC (1.0 mmol, 0.212 g). After 15 minutes ultrasonication, the temperature of the mixture dropped to room temperature, to which another portion of nickelous carbonate (2.0 mmol, 0.3578 g) was added. The mixture was heated at 150 °C in a 40 mL Teflon coated stainless-steel autoclave for 2 h, and then maintained at 120 °C for 22 h. After cooling, the precipitated **Ni-MOF** crystals were collected and rinsed by methanol several times for subsequent processes.

Preparation of porous $Ni(OH)_2$

0.15 g of **Ni-MOF** crystals were immersed in 15 mL of an aqueous solution of KOH with different concentrations (0.5, 1, 6 and 10 M) for 6 hours, and the products were obtained after rinsing with deionized water and ethanol three times in order to remove the residual KOH and the organic ligands. The products were then left at 60 °C for 10 hours.

For investigating the immersion time effects, the **Ni-MOF** crystals were immersed in 15 mL of aqueous KOH solution with a concentration of 6 M for 0.5, 1, 2, 6, and 12 hours. We focused on **$Ni(OH)_2$-6M-6H** for the following reasons: i) a lower concentration drastically expands the soaking time, which is not applicably favorable, and higher concentrations break the MOF skeleton. ii) **$Ni(OH)_2$-6M-6H** presented the best electrochemical performances.

Electrochemical characterizations

All electrochemical tests were conducted on a CHI 760E electrochemical workstation. The measurements were carried out in an ambient environment. In a three electrode system, 6 M KOH, a Hg/HgO electrode, and a (1.5 cm × 1.5 cm) platinum (Pt) foil net were selected as the electrolyte, the reference electrode, and the count electrode, respectively. The working electrode was prepared as follows: $Ni(OH)_2$, carbon black, and polytetra-fluoroethylene (PTFE) as the binder with a mass ratio of 8 : 1 : 1 were ground for 10 min in an agate mortar. Mixed with ethanol, the mixture was ultrasonicated

 This journal is © The Royal Society of Chemistry 2018

Published on 03 July 2018. Downloaded by China university of Petroleum (East China) on 8/25/2018 1:58:30 AM.

for 30 min and then dried in vacuum for 12 hour at 60 °C. 2.5 mg of the mixture was evenly dispersed between two pieces of nickel foam (1 cm × 2 cm). Then each nickel foam was pressed under a pressure of 1 Mpa to obtain the working electrode. The electrochemical properties test mainly relied on cyclic voltammetry (CV) and galvanostatic charge–discharge. Electrochemical impedance spectra were obtained in a 5 mv disturbance voltage, and a frequency impedance below 0.01 to 10^6 Hz.

For the hybrid supercapacitors, $Ni(OH)_2$ was used as the positive electrode, and the activated carbon (AC) electrode was the negative electrode. The AC electrode material was prepared by AC and polytetrafluoroethylene with a mass ratio of 9 : 1. The mixture with the optimized mass was evenly dispersed between two pieces of nickel foam (1 cm × 2 cm), pressed face to face under 1.0 MPa to fabricate the negative electrode. KOH/PVA gel as the solid electrolyte was prepared by mixing 2 g of PVA with 80 ml of deionized water. Heated and stirred until the solution cleared, after which 12 g of KOH was added into the solution under stirring. Finally, after natural volatilization, the KOH/PVA electrolyte gel was obtained.

All the hybrid supercapacitor electrochemical measurements were conducted employing a CHI 760E electrochemical workstation, including cyclic voltammetry (CV) and galvanostatic charge–discharge.

Results and discussion

The successful preparation of the Ni-MOF precursor/template is demonstrated by its XRD pattern shown in Fig. S1.† The schematic for preparing $Ni(OH)_2$ electrodes is shown in Scheme 1. The **Ni-MOF** crystals were immersed in KOH aqueous solutions to produce $Ni(OH)_2$. Herein, the prepared $Ni(OH)_2$ with a concentration of *X* M and an immersion time of *X* hours are denoted as **$Ni(OH)_2$-*X*M-*X*H**. We firstly examined the concentration effects. As shown in Fig. 1a, **$Ni(OH)_2$-*X*M-6H** electrodes present distinct XRD patterns. **$Ni(OH)_2$-0.1M-6H** still has some weak MOF peaks, suggesting an incomplete transformation of the **Ni-MOF** due to the low concentration. From 0.5 to 6 M, no MOF peaks appear in the XRD patterns, and the peaks of $Ni(OH)_2$ clearly increase with KOH concentration. The sharp (100) peak at the 2-theta angle of 33.02° implies the directional growth of $Ni(OH)_2$. The 10 M KOH aqueous solution leads to a poorer crystallization of $Ni(OH)_2$ compared with 6 M KOH. The FTIR measurements show similar results (Fig. 1c). The spectrum for **$Ni(OH)_2$-6M-6H** presents the most intense –OH stretch peak at 3604 cm^{-1}. Moreover, a wide band around 1400 cm^{-1} is observed in all the spectra, and we suggest that this is due to the residual ligands. Therefore, from both the XRD and FTIR results (Fig. 1c), it is concluded that both the higher and lower concentrations lead to a relatively poorer crystallinity.

The effect of the immersion time on $Ni(OH)_2$ formation was examined using 6 M KOH aqueous solution, and the results are presented in Fig. 1b and d. It is obvious that **$Ni(OH)_2$-6M-6H** has stronger XRD peaks and FTIR peaks compared with **$Ni(OH)_2$-6M-0.5H**, and the peaks only slightly grow from 6 to 12 hours, indicating a relatively more crystallized

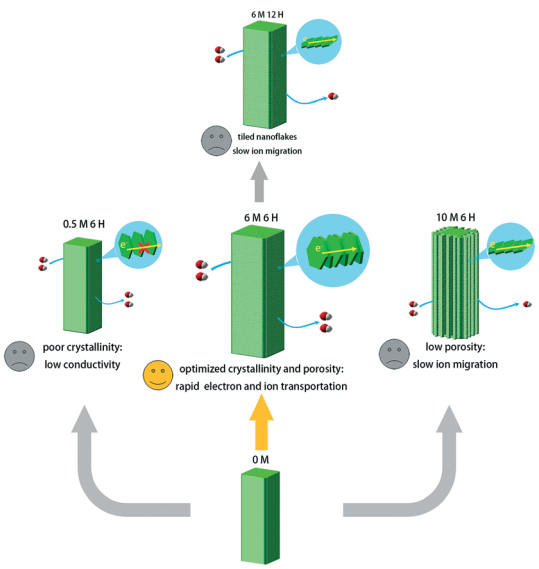

Scheme 1 The proposed alkaline hydrolysis procedure of the **Ni MOF** template at different hydrolysis concentrations of KOH aqueous solutions for 6 h to construct crystalline hierarchical $Ni(OH)_2$ nanostructures.

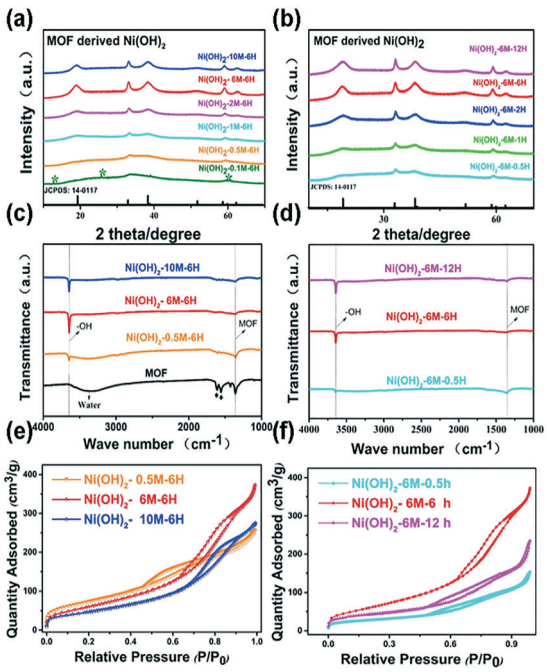

Fig. 1 a) PXRD patterns of $Ni(OH)_2$ prepared with different concentrations, b) PXRD patterns of the $Ni(OH)_2$ prepared with different immersion times, c) FT-IR spectra of **$Ni(OH)_2$-0.5M-6H**, **$Ni(OH)_2$-6M-6H**, **$Ni(OH)_2$-10M-6H**, d) FT-IR spectra of **$Ni(OH)_2$-6M-0.5H**, **$Ni(OH)_2$-6M-6H**, **$Ni(OH)_2$-6M-12H**, e) N_2 adsorption–desorption isotherms of **$Ni(OH)_2$-0.5M-6H**, **$Ni(OH)_2$-6M-6H**, **$Ni(OH)_2$-10M-6H**, f) N_2 adsorption–desorption isotherms of **$Ni(OH)_2$-6M-0.5H**, **$Ni(OH)_2$-6M-6H**, **$Ni(OH)_2$-6M-12H**.

Published on 03 July 2018. Downloaded by China university of Petroleum (East China) on 8/25/2018 1:58:30 AM.

$Ni(OH)_2$ with longer immersion times. TGA and XPS measurements were performed on **$Ni(OH)_2$-6M-6H** to further examine its composition, and the results are shown in Fig. S2 and S3.† The TGA curve indicates that the 17.1% weight loss from room temperature to 250 °C is due to dehydration, and the weight loss of 7.24% above 200 °C is associated with loss of the residual ligands. The XPS plots (Fig. S3†) clearly demonstrate the existence of $Ni(OH)_2$. The Ni 2p band of **$Ni(OH)_2$-6M-6H** is reasonably decomposed into four peaks. The binding energy peak at 854.9 eV and its satellite peak at 860.2 eV are attributed to Ni 2p 3/2, and the binding energy peak at 872.1 eV and its satellite peak at 878.1 eV are attributed to Ni 2p 1/2, with a spin-energy separation of 17.2 eV. Furthermore, a clear C 1s peak also appears at around 298 eV, which further illustrate that organic ligands are within the **$Ni(OH)_2$-6M-6H**.

The porosities of the obtained $Ni(OH)_2$ hierarchical structures were examined by the BET measurements. Nitrogen adsorption–desorption isotherms at 77 K were collected to calculate the specific surface areas (Fig. 1e and f) and pore sizes (Fig. S4†) of the porous $Ni(OH)_2$. As shown in Fig. 1e, $Ni(OH)_2$ obtained from KOH aqueous solutions of different concentrations have distinct isotherms. The **$Ni(OH)_2$-0.5M-6H** has a H4-type hysteresis loop with a BET specific surface area of 274.29 $m^2\ g^{-1}$. **$Ni(OH)_2$-6M-6H** and **$Ni(OH)_2$-10M-6H** exhibit H3-type hysteresis loops (typical of the aggregation of slices), and their specific surface areas are 235.94 $m^2\ g^{-1}$ and 175.54 $m^2\ g^{-1}$, respectively. Fig. 1f demonstrates that the porous structure clearly changes with time. The pores within the **Ni-MOF** were initially constructed with a $Ni(OH)_2$ formation, and the surface area increased from 101.01 $m^2\ g^{-1}$ to 235.94 $m^2\ g^{-1}$. However, the continuous crystallization of $Ni(OH)_2$ lea to closing of the pores and a smaller surface area of 130.81 $m^2\ g^{-1}$.

SEM and TEM images are shown in Fig. 2a–c and S5† to further illustrate the hydrolysis process of the **Ni-MOF** in KOH aqueous solutions with different concentrations. For **$Ni(OH)_2$-0.5M-6H** and **$Ni(OH)_2$-6M-6H**, it is obvious that $Ni(OH)_2$ prepared at a lower concentration possesses the same macro-morphology compared with the **Ni-MOF** template. However, their surfaces show obvious changes. The MOF rods have smooth surfaces, shown in Fig. S5.† After hydrolyzing, cracks and vertically grown $Ni(OH)_2$ nanoflakes bestrewed the surfaces of the rods. Corresponding to the XRD results, the SEM images indicate that fewer $Ni(OH)_2$ nanoflakes formed at a concentration of 0.5 M compared with 6 M. However, the higher concentration is not helpful to the conformal transformation, although it attributes to a larger amount of $Ni(OH)_2$ crystals. The **$Ni(OH)_2$-10M-6H** presents a swelled morphology, and it is difficult to identify individual $Ni(OH)_2$ nanoflakes. The TEM images (Fig. 2d and S6†) give similar results. **$Ni(OH)_2$-6M-6H** is constructed by vertically grown $Ni(OH)_2$ nanoflakes. Abundant $Ni(OH)_2$ nanoflakes with a thickness of around 1 to 2 nm formed during the hydrolysis route, and the obtained structure has a porous morphology. The HRTEM image (Fig. 2e) exhibits the lattice

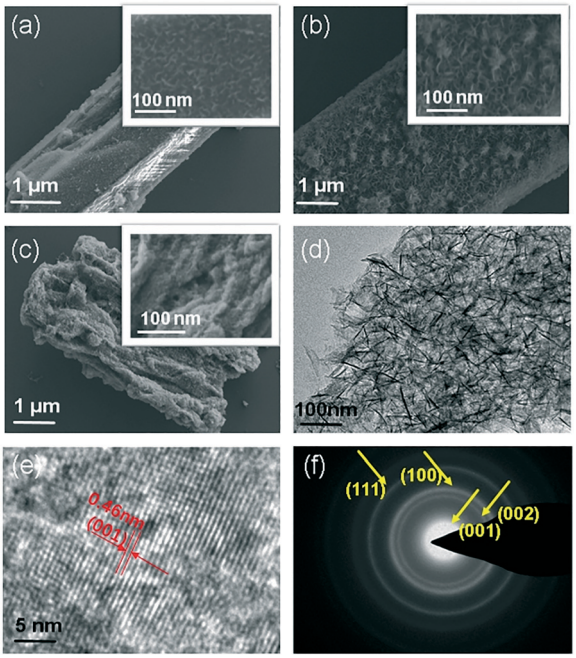

Fig. 2 Morphological characterization of the $Ni(OH)_2$ sample. a–c) SEM images of **$Ni(OH)_2$-0.5M-6H**, **$Ni(OH)_2$-6M-6H** and **$Ni(OH)_2$-10M-6H**, respectively. d–f) TEM images of **$Ni(OH)_2$-6M-6H**.

fringes with d-spacings of 0.46 nm, corresponding to the (001) planes of $Ni(OH)_2$. The SAED image shown in Fig. 2f illustrates the polycrystalline feature. As shown in Fig. S6,† **$Ni(OH)_2$-10M-6H** is constructed of tiled $Ni(OH)_2$ nanoflakes, which is detrimental to the porous structure, and the corresponding BET measurements show that **$Ni(OH)_2$-10M-6H** has a lower surface area. The effects of immersion time are also demonstrated by the TEM images shown in Fig. S7.† **$Ni(OH)_2$-6M-12H** is constructed of tiled $Ni(OH)_2$ nanoflakes, which is supported by the fact that it has a relatively smaller surface area compared with **$Ni(OH)_2$-6M-6H**.

We can then describe the possible hydrolysis route based on the aforementioned analyses. During hydrolysis, the coordination environments of the Ni atoms were changed and the frameworks collapsed initially. Meanwhile, $Ni(OH)_2$ flakes formed and interlaced, fabricating into a 3D hierarchical structure. Higher concentrations of OH^- increased the amounts of $Ni(OH)_2$ nanocrystals and accelerated the crystallization, contributing to smaller sizes of $Ni(OH)_2$ nanocrystals, and meanwhile the rapid reaction of the MOF precursor with OH^- led to a rapid collapse of the MOF skeleton, which was detrimental to the conformal transformation. At the lower concentration, $Ni(OH)_2$ crystallized with MOF collapse simultaneously, contributing to the conformal transformation. Moreover, possibly due to the residual ligands between flakes playing a surfactant-like role, the $Ni(OH)_2$ nanoflakes tended to be vertically grown. With longer immersion, the ligands were further released into the solutions, and the tiled $Ni(OH)_2$ nanoflakes formed eventually.

MOFs have been widely utilized as both templates and precursors to fabricate porous metal oxide/hydroxide

 This journal is © The Royal Society of Chemistry 2018

Published on 03 July 2018. Downloaded by China university of Petroleum (East China) on 8/25/2018 1:58:30 AM.

nanomaterials for supercapacitor applications. The main challenges lie in whether the porous MOF morphology can be maintained for easy ion migration and whether the obtained metal oxide/hydroxides are well crystallized for fast electron transportation. Generally, a relative mild and slow process is preferable to maintain the macro-morphology so that nonequilibrium interdiffusion can be avoided.[34] During the hydrolysis process, by controlling the reaction conditions, the transformation of the **Ni-MOF** into hierarchical $Ni(OH)_2$ can occur in a controllable route, and the morphology maintained. The well dispersed tunnels and pores within porous $Ni(OH)_2$ built during hydrolyzing the MOF precursor allow the full infiltration of the OH^- anions, and the exposed surface areas can be easily accessed. Moreover, the crystallinity of the obtained $Ni(OH)_2$ can be regulated by immersion time and concentration. Therefore, the obtained $Ni(OH)_2$ electrodes with the optimized hydrolyzing conditions are ideal as electrode materials for supercapacitors.

In order to study the electrochemical performances of the MOF-derived hierarchical $Ni(OH)_2$, a three-electrode cell with a 6 M KOH aqueous electrolyte was employed to conduct the CV and galvanostatic charge–discharge measurements. The cyclic voltammogram (CV) curves of all $Ni(OH)_2$ electrodes are shown in Fig. 3a and b, S10 and S11.† The clear redox peaks indicate the battery-type behaviors of the $Ni(OH)_2$ electrodes correspond to conversions between different oxidation states of nickel, which can be described, according to previous reports, as follows.[35]

$$Ni(OH)_2 + OH^- \leftrightarrow NiOOH + H_2O + e^- \quad (1)$$

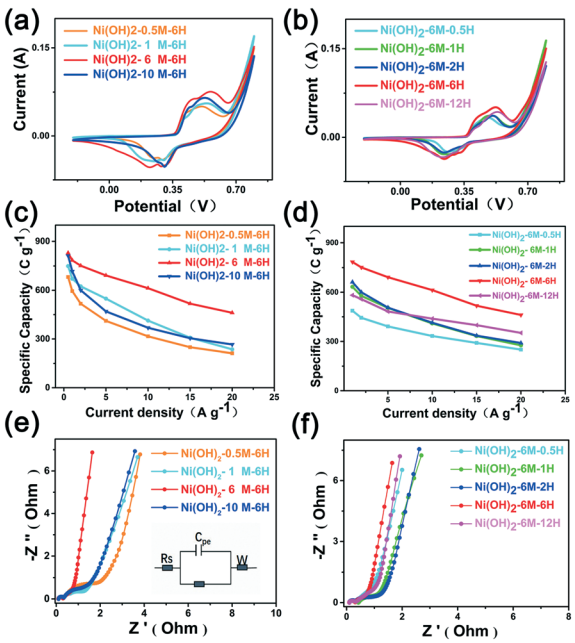

Fig. 3 a and b) CV curves of the as-prepared $Ni(OH)_2$ with different soaking concentrations and different soaking times, c and d) calculated capacity based on the GCD curves of $Ni(OH)_2$ electrodes with different concentrations, e and f) Nyquist plots of the as-prepared $Ni(OH)_2$ electrode, (inset) equivalent circuit.

Galvanostatic measurements were conducted to investigate the charge storage capabilities of $Ni(OH)_2$ electrodes at different charge–discharge currents, and the results are presented in Fig. S8 and S9.† The potential plateaus are associated with the redox peaks, and the symmetric potential-time curves demonstrate a high charge–discharge columbic efficiency. The calculated specific capacity based on the galvanostatic measurements are shown in Fig. 3c and d. As expected, **$Ni(OH)_2$-6M-6H** presented the best electrochemical behaviors. Its specific capacity reached 830.6 C g^{-1} at a current density of 0.5 A g^{-1} and remained at 461.2 C g^{-1} at a current density of 20 A g^{-1}. Meanwhile, **$Ni(OH)_2$-6M-6H** also had a higher specific capacity than many other reported Ni-based electrodes, including Ni-based MOFs (583.08 C g^{-1} at 1 A g^{-1}),[36] **$Ni(OH)_2$ nanosheets** (562.4 C g^{-1} at 1.5 A g^{-1}),[37] **MOF-derived $Ni_xCo_{1-x}(OH)_2$** (494.4 C g^{-1} at 0.5 A g^{-1}),[28] and **$Ni(OH)_2$/graphene** (652.8 C g^{-1} at 1 A g^{-1}).[20] To further investigate the remarkable behaviors of the **$Ni(OH)_2$-6M-6H**, electrochemical impedance spectroscopy (EIS) was used to further analyze the ion diffusion within the electrodes and the interfacial charge/ion transportation between electrodes and electrolytes. The Nyquist plots of all $Ni(OH)_2$ electrodes in the frequency range from 0.01 Hz to 100 kHz are presented in Fig. 3e and f. The fitted results are listed in Table S1.† Herein, R_s represents the electrolyte resistance, and it is expected that the R_s value of all $Ni(OH)_2$ materials will not present any differences.[38] R_{ct} (Faraday resistance) denotes the interfacial charge-transfer resistance at the electrode/electrolyte interfaces and intrinsic charge-transfer resistance of the porous electrode, which is represented by the diameter of the semicircle in the high-frequency region.[39] It is apparent that **$Ni(OH)_2$-6M-6H** has the smallest R_{ct}, implying the lowest intrinsic resistance. At the lower frequency region, the inclined lines imply the diffusion of electrolyte ions within the electrodes. The steep inclined lines of **$Ni(OH)_2$-6M-6H** imply it has least diffusion resistance.

The remarkable electrochemical properties of **$Ni(OH)_2$-6M-6H** are attributed to its optimized hierarchical nanostructures. The intercalation and deintercalation of the hydroxyl ions contribute to its energy storage capability. Therefore, in order to achieve better electrochemical performances, the hierarchical $Ni(OH)_2$ electrode should have large surface areas that the electrolyte can easily access. Meanwhile, it is necessary that $Ni(OH)_2$ is well crystallized to facilitate electron transport. The unique structure and morphology of **$Ni(OH)_2$-6M-6H** satisfy both the requirements. As mentioned above, **$Ni(OH)_2$-6M-6H** produced by hydrolysis of the **Ni-MOF** has proper tunnels which allow the free migration of OH^- anions to easily access the more active sites, and meanwhile interlaced $Ni(OH)_2$ nanoflakes decrease the inner resistance. These features ensure the remarkable electrochemical performances.

In order to illustrate the potential applications of the **$Ni(OH)_2$-6M-6H**, all-solid hybrid supercapacitor was fabricated with **$Ni(OH)_2$-6M-6H** as the anode and activated carbon (AC) as the cathode. The specific capacitance of AC was 150.5 F

Published on 03 July 2018. Downloaded by China university of Petroleum (East China) on 8/25/2018 1:58:30 AM.

g^{-1} at a current density of 1 A g^{-1}, as shown in Fig. S7.† The optimal mass ratio between **the Ni(OH)$_2$-6M-6H** anode and the AC cathode was optimized to 1 : 3.2, as proposed by Zheng, following the charge balance theory (Fig. S12†).[40]

Fig. 4a shows CV curves of the **Ni(OH)$_2$-6M-6H//AC** hybrid supercapacitor device at different voltage windows (0–1.2 V,0–1.3 V,0–1.4 V, 0–1.5 V, 0–1.6 V, and 0–1.7 V) at a scan rate of 25 mV s^{-1}. When the voltage window is extended to 1.7 V, an obvious increase in the current was observed, and plenty of bubbles appeared on the surface of the electrode, which was associated with the OER reaction (oxygen evolution reaction).[41] In order to avoid producing oxygen during charging–discharging and improve the coulomb efficiency of the **Ni(OH)$_2$-6M-6H//AC** hybrid supercapacitor device, a potential window of 0–1.5 V was selected, and the CV curves with different scan rates are shown in Fig. 4b. The shapes of the CV curves of the **Ni(OH)$_2$-6M-6H//AC** hybrid supercapacitor do not change with increasing scan rates, indicating an excellent rate capability. Galvanostatic discharge curves of the **Ni(OH)$_2$-6M-6H//AC** hybrid supercapacitor at a series of current densities and the specific capacitance of the supercapacitor as a function of current density are presented in Fig. 4c and d. The calculated specific capacitances are 100, 84.3, 76, 70.4, 66, 54, and 44.45 F g^{-1} at current densities of 1, 2, 3, 4, 5, 10, and 15 A g^{-1}, respectively, which gradually decrease with increasing charge–discharge current.

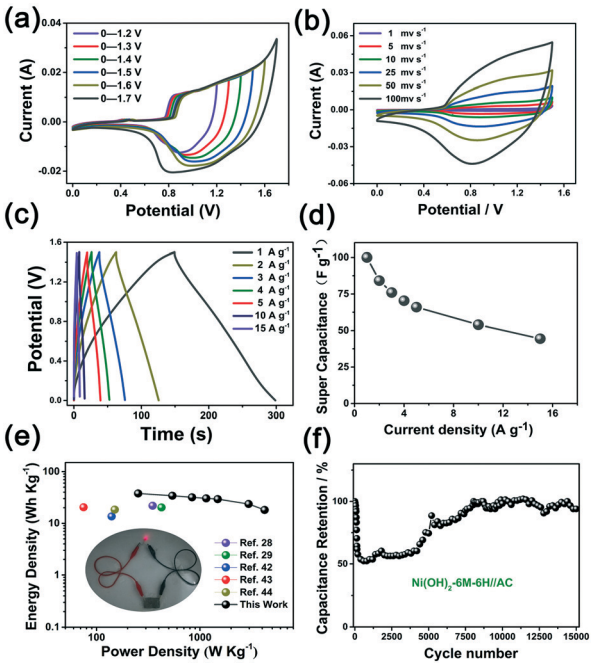

Fig. 4 a) and b) CV curves of the **Ni(OH)$_2$-6M-6H//AC** asymmetric supercapacitor device at different voltage windows and different scan rates; c) charge/discharge curves of the **Ni(OH)$_2$-6M-6H//AC** device at different current densities; d) the specific capacitance as a function of the current densities of the **Ni(OH)$_2$-6M-6H//AC** device; e) Ragone plots of the **Ni(OH)$_2$-6M-6H//AC** asymmetric supercapacitor compared with previously reported results; f) cycling performances of the **NinOH)$_2$-6M-6H//AC** device at 1 A g^{-1}.

The energy density (E) and power density (P) are two major parameters that reveal the electrochemical performances of a full cell. E and P can be calculated *via* the following equations:

$$E = \frac{I}{m}\int_{t1}^{t2} V\mathrm{d}t$$

$$P = \frac{E}{\Delta t}$$

where I is the charge/discharge current density, m is the mass of the electrode materials contained in both electrodes, V is the cell operation potential, and Δt is the time spent in discharge. The **Ni(OH)$_2$-6M-6H//AC** hybrid supercapacitor exhibits an extremely high energy density of 37.8 W h kg^{-1} at a power density of 252.67 W kg^{-1}. To better illustrate the good specific energy and power densities of our hybrid capacitor, a ragone plot (Fig. 4e) showing energy density *versus* power density for various hybrid supercapacitors was made. As indicated, our hybrid supercapacitor devices have better performance compared with MOF-derived **Ni$_x$Co(OH)$_2$ composite//AC** (13.6 W h kg^{-1} at 140 W kg^{-1}),[28] **MOF-derived Co(OH)$_2$//AC** (21.9 W h kg^{-1} at 348.9 W kg^{-1}),[29] **Co–Mn LDH//AC** (20.45 W h kg^{-1} at 75 W kg^{-1}),[42] **Ni(OH)$_2$ nanosheets//AC** (18.4 W h kg^{-1} at 150 W kg^{-1}),[43] and Ni(OH)$_2$ nanoflakes on carbon fibers by chemical bath deposition//AC (20.3 W h kg^{-1} at 425 W kg^{-1}).[44] The cycling performances of the supercapacitor were also investigated. As shown in Fig. 4f, although the capacitance dropped to approximately 50% initially, the capacitance slowly recovered to 93% after 15 000 cycles. Based on reported literature, the capacitance drop has been attributed to several reasons, including phase transformation of the electrode material and the electrode material peeling off the current collector, and the recovery of the capacitance is usually ascribed to wetting of the electrode.[45] However, the dropping and recovering usually occur in the initial several hundred cycles, and thus these statements cannot explain the capacitance rising for our device. We noticed that the initial drop and subsequent increase are common for transition metal based electrodes in lithium ion batteries due to the formation of a polymeric gel-like film associated with the organic electrolyte degradation.[46–48] Considering that there were residual organic ligands within the Ni(OH)$_2$ electrode, we suspect that the initial drop is likely due to the film formed on the electrode surfaces. With increasing cycle time, the film is gradually peeled off, and the capacitance recovers. However, more detailed research about the electrochemical reaction process is still needed. The Nyquist plots of the electrode before and after cycling measurements indicate its good stability, as shown in Fig. S13.†

Conclusions

A simple and facile strategy was employed to fabricate an Ni(OH)$_2$ hierarchical structure for supercapacitor application.

 This journal is © The Royal Society of Chemistry 2018

Published on 03 July 2018. Downloaded by China university of Petroleum (East China) on 8/25/2018 1:58:30 AM.

By soaking the **Ni-MOF** in a 6 M KOH aqueous solution for 6 hours, the $Ni(OH)_2$ hierarchical structure with both an optimized crystallinity for electron transportation and an optimized porous morphology for ion migration was obtained. The optimized $Ni(OH)_2$ electrode presents a remarkable charge storage behavior with a specific capacity of 830.6 C g^{-1} at 0.5 A g^{-1}. The fabricated all-solid state asymmetric supercapacitor presents a remarkable energy density and power density of 37.8 W h kg^{-1} and 252.67 W kg^{-1}, respectively. The cycling test indicates that 93% of the initial capacitance was retained after 15 000 cycles, illustrating the remarkable long-life performance.

Conflicts of interest

There are no conflicts to declare.

Acknowledgements

This work was supported by the NSFC (Grant No. 21571187 and 21571137) and a Taishan Scholar Foundation (ts201511019).

References

1 J. W. Choi and D. Aurbach, *Nat. Rev. Mater.*, 2016, **1**, 16013.
2 Y. Wang, K. S. Chen, J. Mishler, S. C. Cho and X. C. Adroher, *Appl. Energy*, 2011, **88**, 981–1007.
3 L. L. Zhang and X. S. Zhao, *Chem. Soc. Rev.*, 2009, **38**, 2520–2531.
4 B. Y. Guan, X. Y. Yu, H. B. Wu and X. W. D. Lou, *Adv. Mater.*, 2017, **29**, 1703614.
5 B. Liu, H. Shioyama, H. Jiang, X. Zhang and Q. Xu, *Carbon*, 2010, **48**, 456–463.
6 Z. Jiang, Z. Li, Z. Qin, H. Sun, X. Jiao and D. Chen, *Nanoscale*, 2013, **5**, 11770–11775.
7 P. Sharma and T. S. Bhatti, *Energy Convers. Manage.*, 2010, **51**, 2901–2912.
8 A. Burke, *J. Power Sources*, 2000, **91**, 37–50.
9 R. R. Salunkhe, C. Young, J. Tang, T. Takei, Y. Ide, N. Kobayashi and Y. Yamauchi, *Chem. Commun.*, 2016, **52**, 4764–4767.
10 X. Lu, Y. Hu, L. Wang, Q. Guo, S. Chen, S. Chen, H. Hou and Y. Song, *Electrochim. Acta*, 2016, **189**, 158–165.
11 D. Jiang, C. Li, W. Yang, J. Zhang and J. Liu, *J. Mater. Chem. A*, 2017, **5**, 18684–18690.
12 C. Choi, J. A. Lee, A. Y. Choi, Y. T. Kim, X. Lepro, M. D. Lima, R. H. Baughman and S. J. Kim, *Adv. Mater.*, 2014, **26**, 2059–2065.
13 B. Song, X. Cui, Y. Xie, S. Cheng, Y. Shao and Y. Sun, *Cryst. Growth Des.*, 2017, 3548–3555.
14 X. Lv, H. Zhang, F. Wang, Z. Hu, Y. Zhang, L. Zhang, R. Xie and J. Ji, *CrystEngComm*, 2018, **20**, 1690–1697.
15 L. Wang, J. Yu, X. Dong, X. Li, Y. Xie, S. Chen, P. Li, H. Hou and Y. Song, *ACS Sustainable Chem. Eng.*, 2016, **4**, 1531–1537.
16 R. T. Wang, L. B. Kong, J. W. Lang, X. W. Wang, S. Q. Fan, Y. C. Luo and L. Kang, *J. Power Sources*, 2012, **217**, 358–363.
17 S. Zheng, X. Li, B. Yan, Q. Hu, Y. Xu, X. Xiao, H. Xue and H. Pang, *Adv. Energy Mater.*, 2017, **7**, 1602733.
18 K. Ding, X. Zhang, J. Li, P. Yang and X. Cheng, *CrystEngComm*, 2017, **19**, 5780–5786.
19 J. Yan, Z. Fan, W. Sun, G. Ning, T. Wei, Q. Zhang, R. Zhang, L. Zhi and F. Wei, *Adv. Funct. Mater.*, 2012, **22**, 2632–2641.
20 R. Wang, A. Jayakumar, C. Xu and J. M. Lee, *ACS Sustainable Chem. Eng.*, 2016, **4**, 3736–3742.
21 J. Zhao and Q. Zhang, *Electrochim. Acta*, 2015, **184**, 47–57.
22 H. C. Zhou and S. Kitagawa, *Chem. Soc. Rev.*, 2014, **43**, 5415–5418.
23 X. Xiong, L. Zhou, W. Cao, J. Liang, Y. Wang, S. Hu, F. Yu and B. Li, *CrystEngComm*, 2017, **19**, 7177–7184.
24 W. Chaikittisilp, N. L. Torad, C. Li, M. Imura, N. Suzuki, S. Ishihara, K. Ariga and Y. Yamauchi, *Chemistry*, 2014, **20**, 4217–4221.
25 J. Tang and Y. Yamauchi, *Nat. Chem.*, 2016, **8**, 638–639.
26 W. Zhang, X. Jiang, Y. Zhao, A. Carne Sanchez, V. Malgras, J. Kim, J. H. Kim, S. Wang, J. Liu, J. S. Jiang, Y. Yamauchi and M. Hu, *Chem. Sci.*, 2017, **8**, 3538–3546.
27 P. Wen, P. Gong, J. Sun, J. Wang and S. Yang, *J. Mater. Chem. A*, 2015, **3**, 13874–13883.
28 S. He, Z. Li, J. Wang, P. Wen, J. Gao, L. Ma, Z. Yang and S. Yang, *RSC Adv.*, 2016, **6**, 49478–49486.
29 Z. Wang, Y. Liu, C. Gao, H. Jiang and J. Zhang, *J. Mater. Chem. A*, 2015, **3**, 20658–20663.
30 L. Wang, H. Yang, G. Pan, L. Miao, S. Chen and Y. Song, *Electrochim. Acta*, 2017, **240**, 16–23.
31 D. O. Miles, D. Jiang, A. D. Burrows, J. E. Halls and F. Marken, *Electrochem. Commun.*, 2013, **27**, 9–13.
32 Z. Xiao, L. Fan, B. Xu, S. Zhang, W. Kang, Z. Kang, H. Lin, X. Liu, S. Zhang and D. Sun, *ACS Appl. Mater. Interfaces*, 2017, **9**, 41827–41836.
33 H. J. Yang, A. L. Cui, R. J. Wang and H. Z. Kou, *Chin. J. Chem.*, 2008, 1527–1531.
34 J. A. Greathouse and M. D. Allendorf, *J. Am. Chem. Soc.*, 2006, 10678–10679.
35 B. K. Kim, V. Chabot and A. Yu, *Electrochim. Acta*, 2013, **109**, 370–380.
36 Y. Zhou, Z. Mao, W. Wang, Z. Yang and X. Liu, *ACS Appl. Mater. Interfaces*, 2016, **8**, 28904–28916.
37 Z. Li, W. Zhang, Y. Su, H. Wang and B. Yang, *Appl. Surf. Sci.*, 2016, **383**, 268–275.
38 M. S. Javed, S. Dai, M. Wang, D. Guo, L. Chen, X. Wang, C. Hu and Y. Xi, *J. Power Sources*, 2015, **285**, 63–69.
39 C. Huang, J. Zhang, N. P. Young, H. J. Snaith and P. S. Grant, *Sci. Rep.*, 2016, **6**, 25684.
40 Z. Jim and P. Zheng, *J. Electrochem. Soc.*, 2003, **2150**, A2484–A2492.

Published on 03 July 2018. Downloaded by China university of Petroleum (East China) on 8/25/2018 1:58:30 AM.

41 M. B. Stevens, L. J. Enman, A. S. Batchellor, M. R. Cosby, A. E. Vise, C. D. M. Trang and S. W. Boettcher, *Chem. Mater.*, 2016, **29**, 120–140.
42 F. O. Ochai-Ejeh, M. J. Madito, D. Y. Momodu, A. A. Khaleed, O. Olaniyan and N. Manyala, *Electrochim. Acta*, 2017, **252**, 41–54.
43 Y. Mao, T. Li, C. Guo, F. Zhu, C. Zhang, Y. Wei and L. Hou, *Electrochim. Acta*, 2016, **211**, 44–51.
44 N. A. Alhebshi, R. B. Rakhi and H. N. Alshareef, *J. Mater. Chem. A*, 2013, **1**, 14897.
45 Y. Chen, W. K. Pang, H. Bai, T. Zhou, Y. Liu, S. Li and Z. Guo, *Nano Lett.*, 2017, **17**, 429–436.
46 W. Tian, H. Hu, Y. Wang, P. Li, J. Liu, J. Liu, X. Wang, X. Xu, Z. Li, Q. Zhao, H. Ning, W. Wu and M. Wu, *ACS Nano*, 2018, **12**, 1990–2000.
47 S. Hao, B. Zhang, S. Ball, J. Wu, M. Srinivasan and Y. Huang, *J. Mater. Chem. A*, 2016, **4**, 16569–16575.
48 G. Hu, C. Li and H. Gong, *J. Power Sources*, 2010, **195**, 6977–6981.

 This journal is © The Royal Society of Chemistry 2018